RESEARCH ARTICLE
Editor's Choice
ADVANCED MATERIALS INTERFACES Open Access
www.advmatinterfaces.de

Check for updates

Controlled Fabrication of Native Ultra-Thin Amorphous Gallium Oxide From 2D Gallium Sulfide for Emerging Electronic Applications

*AbdulAziz AlMutairi, Aferdita Xhameni, Xuyun Guo, Irina Chircă, Valeria Nicolosi, Stephan Hofmann, and Antonio Lombardo**

Oxidation of 2D layered materials has proven advantageous in creating oxide/2D material heterostructures, opening the door for a new paradigm of low-power electronic devices. Gallium (II) sulfide (β-GaS), a hexagonal phase group III monochalcogenide, is a wide bandgap semiconductor with a bandgap exceeding 3 eV in single and few-layer form. Its oxide, gallium oxide (Ga_2O_3), combines a large bandgap (4.4–5.3 eV) with a high dielectric constant (≈10). Despite the technological potential of both materials, controlled oxidation of atomically-thin β-GaS remains under-explored. This study focuses on the controlled oxidation of β-GaS using oxygen plasma treatment, addressing a significant gap in existing research. The results demonstrate the ability to form ultrathin native oxide (GaS_xO_y), 4 nm in thickness, upon exposure to 10 W of O_2, resulting in a GaS_xO_y/GaS heterostructure where the GaS layer beneath remains intact. By integrating such structures between metal electrodes and applying electric stresses as voltage ramps or pulses, their use for resistive random-access memory (ReRAM) is investigated. The ultrathin nature of the produced oxide enables low operation power with energy use as low as 0.22 nJ per operation while maintaining endurance and retention of 350 cycles and 10^4 s, respectively. These results show the significant potential of the oxidation-based GaS_xO_y/GaS heterostructure for electronic applications and, in particular, low-power memory devices.

1. Introduction

Gallium oxide (Ga_2O_3), a wide bandgap semiconductor, has emerged as a material of significant interest to the semiconductor industry owing to its excellent chemical and electrical properties. Its wide bandgap of 4.4–5.3 eV,[1–5] in addition to its thermal and chemical stability, made Ga_2O_3 applications in electronics very versatile. Notably, β-Ga_2O_3 boasts a high breakdown field strength of up to 8 MV cm^{-1},[6] a fact that fuelled the investigation into its applications in high-power electronics. Beyond conventional electronics, Ga_2O_3 has demonstrated tremendous potential in resistive switching (RS) applications due to its high intrinsic resistance and sensitivity to oxygen content.[7–9] The latter is more predominantly observed in amorphous Ga_2O_3, and low-power uni- and bipolar switching has been achieved in Ga_2O_3 memristors.[10–16]

Nevertheless, the fabrication of ultra-thin, high-quality film of Ga_2O_3 remains

A. AlMutairi, I. Chircă, S. Hofmann
Department of Engineering
University of Cambridge
Cambridge CB2 1PZ, UK

A. AlMutairi, A. Xhameni, A. Lombardo
London Centre for Nanotechnology
19 Gordon St, London WC1H 0AH, UK
E-mail: a.lombardo@ucl.ac.uk

The ORCID identification number(s) for the author(s) of this article can be found under https://doi.org/10.1002/admi.202400481

© 2024 The Author(s). Advanced Materials Interfaces published by Wiley-VCH GmbH. This is an open access article under the terms of the Creative Commons Attribution License, which permits use, distribution and reproduction in any medium, provided the original work is properly cited.

DOI: 10.1002/admi.202400481

A. Xhameni, A. Lombardo
Department of Electronic & Electrical Engineering
Malet Place
University College London
London WC1E 7JE, UK

X. Guo, V. Nicolosi
Advanced Materials and BioEngineering Research (AMBER)
Centre at Trinity College Dublin and the Royal College of Surgeons in Ireland
Dublin 2 D02 PN40, Ireland

X. Guo, V. Nicolosi
Trinity Centre for Biomedical Engineering
Trinity College Dublin
Dublin 2 D02 PN40, Ireland

X. Guo, V. Nicolosi
School of Chemistry
Trinity College Dublin
Dublin 2 D02 PN40, Ireland

ADVANCED MATERIALS INTERFACES
Open Access
www.advmatinterfaces.de

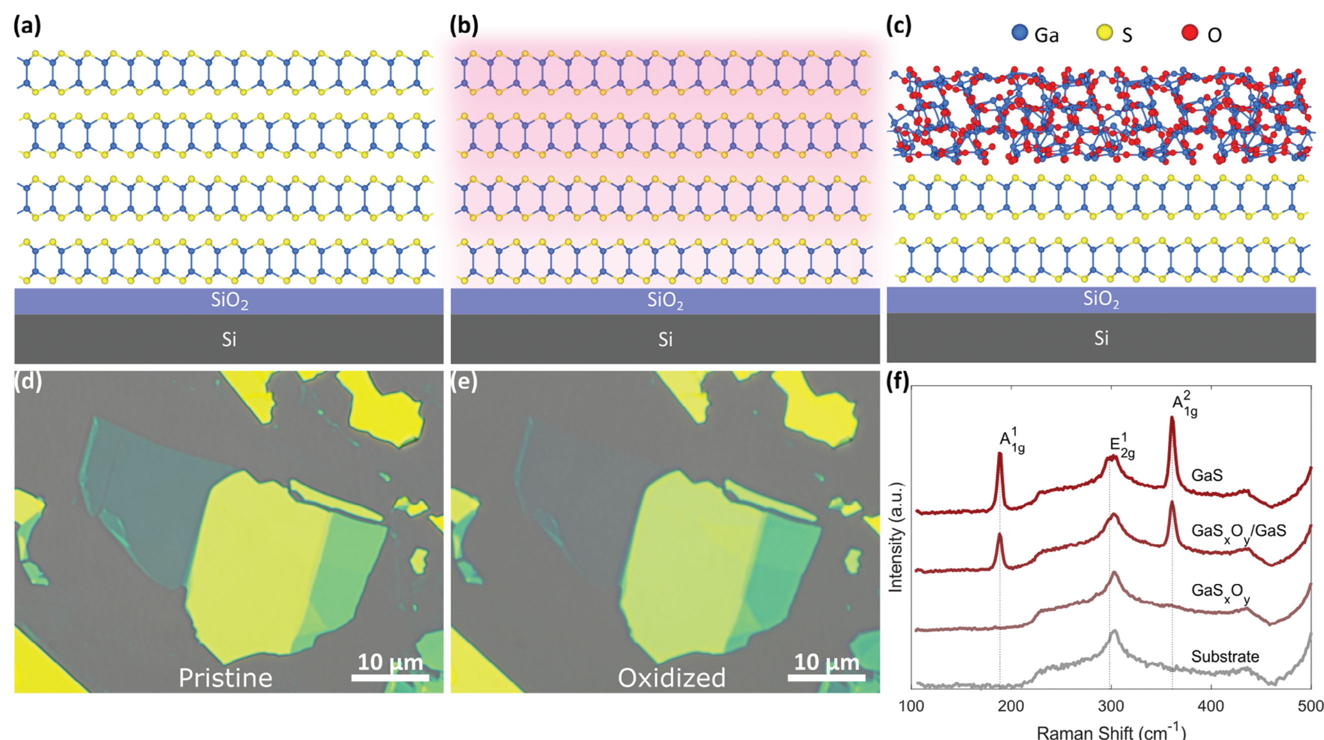

Figure 1. Schematic representation of the oxidation process in GaS. a) Exfoliation of the GaS flake onto a SiO_2/Si substrate. b) Oxygen plasma exposure of the exfoliated GaS flake. c) Conversion of the topmost layers into GaS_xO_y. d,e) Optical microscope images of a pristine and an oxidized GaS flake which was oxidized at 10 W of O_2 plasma at 10 sccm and 20 mTorr for 15 min, respectively, demonstrating a color change post oxidation. The substrate is Si with 285 nm SiO_2. f) Raman spectra of three different GaS flakes and the base SiO_2/Si substrate spectrum. The pristine GaS and the partially oxidized GaS_xO_y/GaS show the characteristic $A^1{}_{1g}$, $A^2{}_{1g}$, and $E^1{}_{2g}$ peaks, whereas the fully oxidized GaS_xO_y shows no characteristic GaS peaks.

a challenge. To this end, several techniques have been explored, such as the mechanical exfoliation of large Ga_2O_3 crystals and the squeezing of liquid Gallium metal.[15–17] However, the previously reported techniques, while promising, still face many challenges, such as the potential for scalability. A rarely explored scalable approach to obtain ultra-thin Ga_2O_3 is through the oxidation of a 2D layered material containing Ga metal.[18] Oxidation of 2D materials has been shown to produce ultra-thin oxides with high dielectric constants and clean interfaces in materials such as HfS_2,[19,20] $HfSe_2$,[21] TaS_2,[22] $ZrSe_2$,[21] and Bi_2O_2Se.[23] Oxidation techniques spanning thermal,[21–23] oxygen plasma,[19,20] and photo-oxidation [24] have been explored, with plasma oxidation standing out for its ability to produce uniform dielectric layers. Furthermore, using a standard resist mask, it allows precise control of the location of oxidation, offering enhanced fabrication flexibility and tailored device functionality.

Group III monochalcogenides layered materials in X-M-M-X (M = Ga, In and X = S, Se, Te) form present a promising platform for electronic device applications.[25–28] More importantly, it has been reported that a good number of Ga-based group III monochalcogenides form a stable native Ga_2O_3.[29,30] One of the members of the monochalcogenides group that is generally neglected is hexagonal-layered gallium (II) sulfide (GaS), commonly referred to as β-GaS. A wide bandgap 2D material, GaS, has found its footing in applications such as optoelectronics.[25,26,31] In line with other layered monochalcogenides, GaS can be oxidized despite its oxidation not being as rapid as GaSe or InSe.[18] However, reports on the oxidation mechanism of GaS are scarce and primarily focus on incidental environmental exposure rather than controlled oxidative processes.[18]

This study investigates gallium oxide (GaS_xO_y) and GaS_xO_y/GaS structures produced by oxidizing GaS via plasma oxidation under carefully controlled conditions and their use in resistive memories. Plasma oxidation of GaS resulted in ultra-thin amorphous GaS_xO_y while keeping the GaS layers beneath intact. Resistive-random-access memory (ReRAM) based on GaS_xO_y/GaS heterostructure exhibited low switching voltages and respectable endurance and retention.

2. Results and Discussion

Figure 1a–c shows a schematic of the GaS oxidation process using radio frequency (RF) oxygen plasma at room temperature. Multilayer GaS flakes are mechanically exfoliated (as described in the experimental section) on a SiO_2/Si substrate. The flakes are then exposed to 10 W of O_2 plasma at 10 sccm and 20 mTorr, which alters the top layers of the flake chemically by converting them into a thin oxide layer. The chemical alteration can be deduced optically by observing a color change in the flake post-oxidation in which the color appears more translucent as the thickness of the oxide increases (Figure 1d,e). The final product could be partially or fully oxidized, depending on the oxidation conditions, time, and the initial GaS flake thickness.

© 2024 The Author(s). Advanced Materials Interfaces published by Wiley-VCH GmbH

21967350, 0, Downloaded from https://onlinelibrary.wiley.com/doi/10.1002/admi.202400481 by University College London UCL Library Services, Wiley Online Library on [28/08/2024]. See the Terms and Conditions (https://onlinelibrary.wiley.com/terms-and-conditions) on Wiley Online Library for rules of use; OA articles are governed by the applicable Creative Commons License

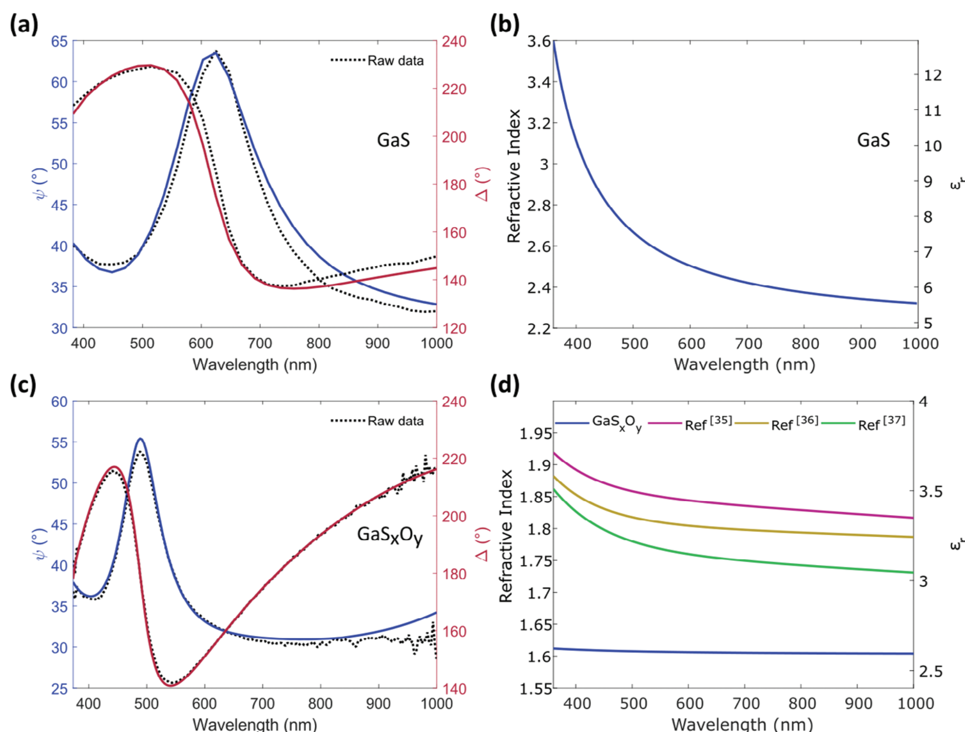

Figure 2. Spectroscopic imaging ellipsometry (SIE) of GaS and GaS_xO_y. a) ψ and Δ spectra fitted using the Tauc–Lorentz oscillator model (A = 94.3 ± 17.2 eV, E_0 = 4.133 ± 0.004 eV, E_g = 2.44 ± 0.15 eV, and Γ = 0.05 ± 1 eV). (b) Corresponding refractive index and real part of the dielectric response. c) ψ and Δ spectra of GaS_xO_y fitted using the Cauchy dispersion model (A = 1.603 ± 0.005, B = 1177 ± 1327 nm^2, C = 0 ± 1 nm^4). d) Refractive index and the corresponding real part of the dielectric response of the GaS_xO_y. Previously reported refractive index of amorphous Ga_2O_3 are included for comparison.[35–37]

Figure 1f shows the Raman spectra of three GaS flakes at different oxidation levels, which are pristine, partially oxidized, and fully oxidized in addition to the spectrum of the SiO_2/Si substrate for reference. While both pristine and partially oxidized GaS show the characteristic $A^1{}_{1g}$, $A^2{}_{1g}$, and $E^1{}_{2g}$ peaks, fully oxidized flake shows no characteristic peaks of GaS, as shown in Figure 1f.

To further characterize GaS and GaS_xO_y, spectroscopic imaging ellipsometry (SIE) was utilized as it has been proven crucial to studying similar material systems.[32] To this end, A ≈10.3 nm pristine GaS flake (kept in an oxygen-free environment during measurement) and a fully oxidized ≈2.4 nm GaS_xO_y (both exfoliated on SiO_2/Si substrate) were used for the measurements. The Tauc–Lorentz oscillator model was employed to fit the GaS data,[33] whereas the Cauchy dispersion model was utilized for the GaS_xO_y.

Figure 2a shows the Tauc-Lorentz oscillator model fit of the ψ and Δ of the GaS resulting in the following fitting parameters A = 94.3 ± 17.2 eV, E_0 = 4.133 ± 0.004 eV, E_g = 2.44 ± 0.15 eV, and Γ = 0.05 ± 1 eV. From the model, the bandgap was estimated to be 2.44 ± 0.15 eV, which is in good agreement with previous reports.[31,34] Due to the limited energy range used for this measurement, no interband transition peaks were observed in the dielectric response (Figure 2b). The Cauchy dispersion, shown in Figure 2c, with fitting parameter = 1.603 ± 0.005, B = 1177 ± 1327 nm^2, C = 0 ± 1 nm^4 fits well to the transparent GaS_xO_y. The refractive index (n), shown in Figure 2d, differs from the typical refractive index reported for amorphous Ga_2O_3. For example, at 600 nm wavelength, fully oxidized GaS_xO_y exhibits n ≈1.6, whereas the n value reported in the literature for amorphous Ga_2O_3 sits in the range of 1.75–1.9.[35–37] This observation suggests that the oxidized GaS is of lower density, leading to a lower refractive index.[38]

To further investigate the structure and chemical composition of the oxide, transmission electron microscopy (TEM) has been employed in conjunction with electron energy loss spectroscopy (EELS) measurements. The TEM results provide an understanding of the material's atomic arrangements, while EELS maps provide the elemental distributions, allowing a better understanding of the formed oxide nature. **Figure 3a,b** shows the cross-sectional TEM image of a partially oxidized GaS flake, subjected to 15-min oxidation, distinctly showing the formation of an oxide/semiconductor (GaS_xO_y/GaS) heterostructure with an oxide thickness of roughly 4 nm. The oxide derived in this manner is amorphous in nature, similar to oxides produced by oxygen plasma oxidation of other 2D materials.[19,39] Notably, the plasma oxidation does not damage the lattice of the unoxidized GaS which appears beneath the oxidized GaS. This is confirmed by in-plane TEM images of partially oxidized GaS flake, which were transferred on a Silicon Nitride (SiN_x) TEM grid before the oxidation. Here, the unoxidized GaS retains its inherent hexagonal crystalline structure, with the damage appearing minimal (Figure 3c). This observation aligns well with the diffraction patterns presented in Figure 3d. In Figure 3e, we show the

© 2024 The Author(s). Advanced Materials Interfaces published by Wiley-VCH GmbH

21967350, 0, Downloaded from https://onlinelibrary.wiley.com/doi/10.1002/admi.202400481 by University College London UCL Library Services, Wiley Online Library on [28/08/2024]. See the Terms and Conditions (https://onlinelibrary.wiley.com/terms-and-conditions) on Wiley Online Library for rules of use; OA articles are governed by the applicable Creative Commons License

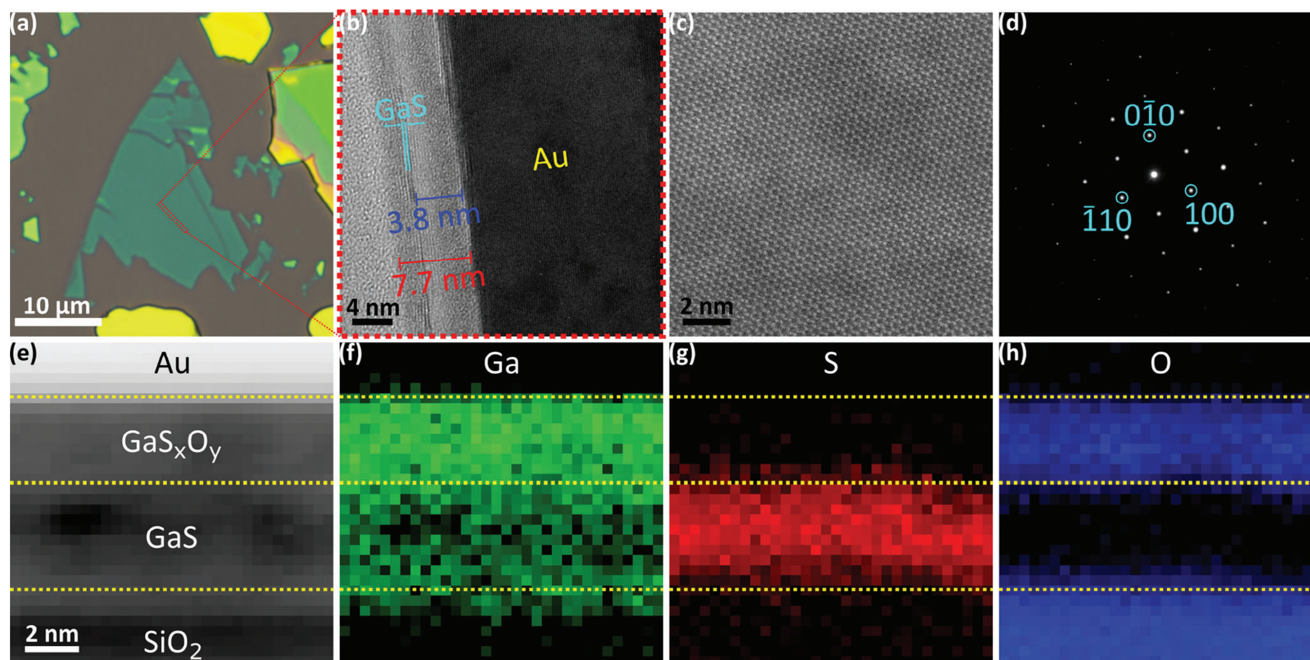

Figure 3. TEM images of partially oxidized GaS flake that was oxidized for 15 mins. a,b) Optical image of the GaS_xO_y/GaS flake and its corresponding cross-section TEM image. The TEM image shows the formation of an amorphous layer on top of the crystalline GaS. c,d) HR-STEM image of a GaS_xO_y/GaS flake and its diffraction pattern confirming that the unoxidized GaS layers exhibit minimal damage. e–h) HAADF-STEM image and its EELS elemental map of the flake from (a) showing the dominant sulfur and oxygen domain corresponding to the unoxidized GaS and the GaS_xO_y layers, respectively.

high-angle annular dark-field scanning TEM (HAADF-STEM) region from the same partially oxidized GaS flake as shown in Figure 3a,b. Figure 3f–h presents the EELS elemental maps for Ga, S, and O corresponding to the imaged region in Figure 3e. These EELS results corroborate our earlier assertion that the partially oxidized GaS forms an oxide/semiconductor (GaS_xO_y/GaS) heterostructure, where the top layer undergoes oxidation while the bottom layer is minimally changed. However, the results also demonstrate that while there is a clear separation between the GaS and the GaS_xO_y layers, the GaS_xO_y still contains some sulfur species, as shown in Figure 3g, and hence the designation GaS_xO_y.

As shown in **Figure** 4a,b, the TEM images of the GaS_xO_y produced at different oxidation times indicate that the oxide thickness after 10 and 15 min of oxidation is almost indistinguishable, which could indicate a self-limiting mechanism for oxidation at the given oxidation parameters. The average oxide thickness for both oxidation times was found to be ≈3.8 nm, with a standard deviation of ≈0.37 nm (Figure 4c). In the context of device fabrication, the oxidation technique demonstrated here presents a

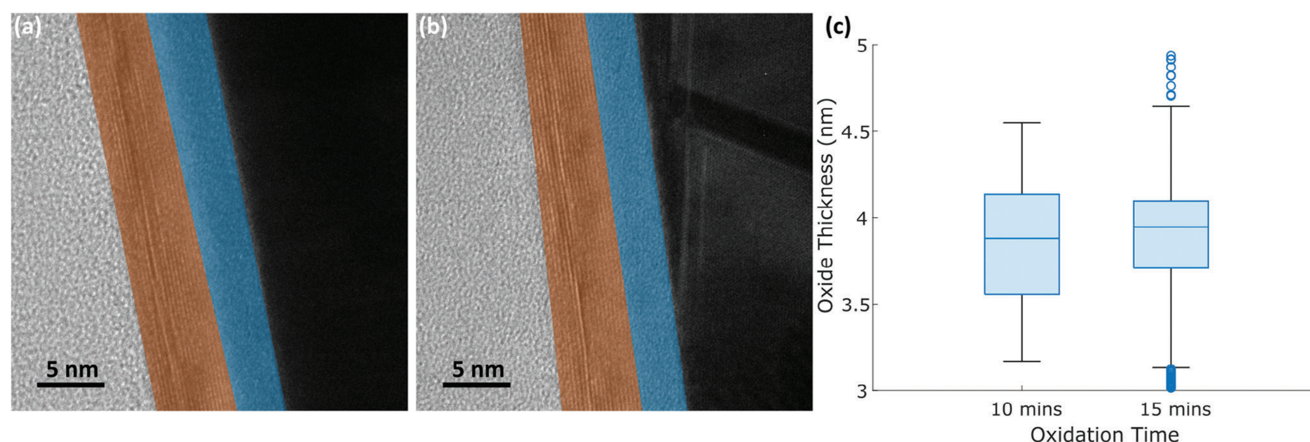

Figure 4. Time-dependent oxide thickness. a,b) False color TEM cross-sectional images of 10 and 15 min oxidation time, respectively. The GaS region is highlighted in orange, while the GaS_xO_y region is highlighted in blue. c) The calculated oxide thicknesses of 10 and 15 min oxidation demonstrate near identical average and distribution (open circles are for thickness outliers).

© 2024 The Author(s). Advanced Materials Interfaces published by Wiley-VCH GmbH

21967350, 0, Downloaded from https://onlinelibrary.wiley.com/doi/10.1002/admi.202400481 by University College London UCL Library Services, Wiley Online Library on [28/08/2024]. See the Terms and Conditions (https://onlinelibrary.wiley.com/terms-and-conditions) on Wiley Online Library for rules of use; OA articles are governed by the applicable Creative Commons License

21967350, 0, Downloaded from https://onlinelibrary.wiley.com/doi/10.1002/admi.202400481 by University College London UCL Library Services, Wiley Online Library on [28/08/2024]. See the Terms and Conditions (https://onlinelibrary.wiley.com/terms-and-conditions) on Wiley Online Library for rules of use; OA articles are governed by the applicable Creative Commons License

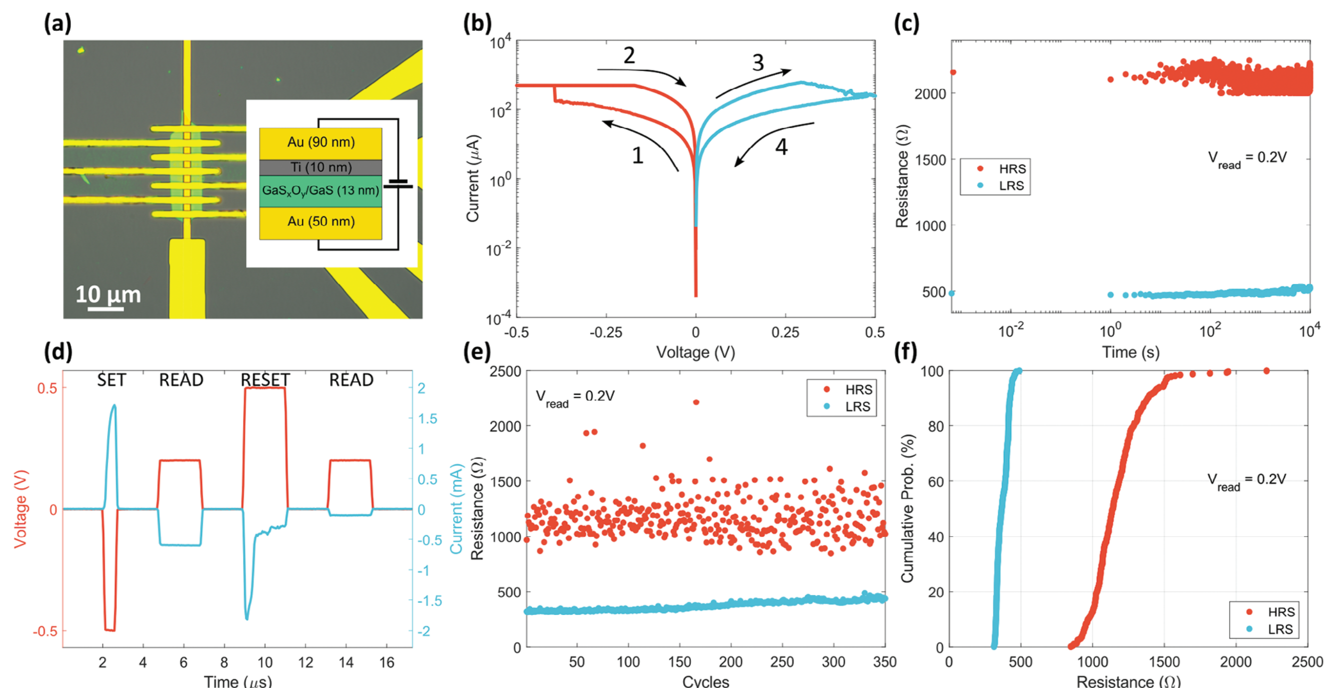

Figure 5. Oxidized GaS-based ReRAM element electrical characterization. a) Optical image of ReRAM element showing common bottom electrode with multiple top electrodes. Inset is a schematic of the vertical stack ReRAM. b) Typical DC switch cycle of ReRAM device where the device switches from HRS to LRS in the negative voltage regime and from LRS to HRS when voltage polarity changes. c) Resistance state retention over time measured at 0.2 V showing stable separation between HRS and LRS for 10^4 s. d) Representative single PVS SET and RESET measurement cycle of voltage and current showing a SET step followed by READ, and a RESET step followed by another READ. e,f) Endurance measurement and corresponding CDF plots read at 0.2 V.

significant advantage by reliably producing ultra-thin oxide layers while exhibiting a wide tolerance for variations in oxidation times.

In the landscape of low-power electronics, the push for more efficient, compact, and faster memory technologies has been endless. Memristors stand out in this domain as promising candidates due to their unique ability to retain their resistance state based on applied voltage or current history.[40] At the forefront of this innovative frontier is the ReRAM, a distinct paradigm of switching memory technology. Beyond their evident advantages in terms of speed, endurance, and device density, ReRAM devices present a deceptively simple architecture.[41–44] This convergence of attributes makes ReRAM a key candidate for leading the advancement in low-power memory systems. Conventionally sputtered or deposited Ga_2O_3 has shown great potential in resistive switching applications with both uni- and bipolar behavior observed.[10–14,16] In addition, recently, partially oxidized 2D materials such as HfS_2, $HfSe_2$, and $PdSe_2$ have shown promise for these applications,[39,45–47] which motivated us to explore the use of the GaS_xO_y/GaS heterostructure in ReRAM applications.

As described in the experimental section, the GaS_xO_y/GaS ReRAMs were fabricated using a 50 nm gold (Au) bottom electrode and a 90/10 nm Au/Ti top electrode. Due to the small footprint of each device (≈4 µm^2), multiple devices were made from the same flake. However, rather than using a standard crossbar array of multiple write lines (WL) and bit lines (BL), we used a single common BL to avoid sneak current paths from forming, as shown in **Figure 5**a. Figure 5b shows typical direct current (DC) *I–V* characteristics of GaS_xO_y/GaS ReRAM oxidized for 10 min where the voltage bias is applied to the bottom electrode. The device exhibits a bipolar switching behavior, switching from a high resistive state (HRS) to a low resistive state (LRS) with a negative DC *I–V* sweep and from LRS to HRS using a positive DC sweep. The low SET (V_{SET}) and RESET voltages (V_{RESET}) of −0.4 and 0.3 V, respectively, can be attributed to several factors such as the ultra-thin (≈4 nm) and low-density nature of the oxide in addition to the presence of mobile oxygen and sulfur ions. We note that all 6 tested GaS_xO_y/GaS ReRAMs with Au/Ti top electrodes start in LRS and, therefore, do not require a forming step, which is normally required for resistive memories.[48–50] This can be advantageous for resistive device applications as it eliminates the need for a separate circuit responsible for the forming step. While the reason behind the forming-free behavior is still unclear, it can be speculated that this could be a result of the lower density of the oxide and the potential access of mobile ions within the switching layer. To further investigate the GaS_xO_y/GaS ReRAM device performance, retention measurements were conducted. The device exhibits good retention at 0.2 V READ voltage, where we can see a clear separation of the resistive states for 10^4 s (Figure 5c). To characterize the device switching behavior, the pulsed voltage stress (PVS) measurements approach was chosen. PVS measurements were performed by applying 500 ns, −0.5 V SET pulses, and 2 µs, 0.5 V RESET pulses on a different device on the same flake. The resistance was read using 2 µs, 0.2 V pulses having a 100 ns rise and fall time and 2 µs separation time, as shown in Figure 5d. As shown in Figure 5e, the

 © 2024 The Author(s). Advanced Materials Interfaces published by Wiley-VCH GmbH

21967350, 0, Downloaded from https://onlinelibrary.wiley.com/doi/10.1002/admi.202400481 by University College London UCL Library Services, Wiley Online Library on [28/08/2024]. See the Terms and Conditions (https://onlinelibrary.wiley.com/terms-and-conditions) on Wiley Online Library for rules of use; OA articles are governed by the applicable Creative Commons License

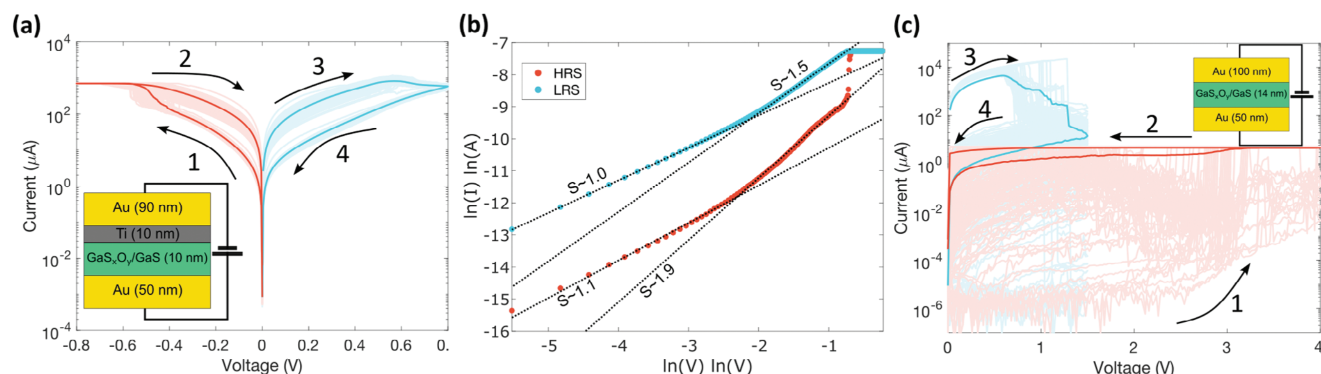

Figure 6. Electrode role in device switching in GaS_xO_y/GaS ReRAM. a) IV sweeps of the devices with light colors representing the cycles and the saturated color curves representing the average. Inset is a schematic of the vertical stack ReRAM with 10 nm GaS_xO_y/GaS. b) ln(I) versus ln(V) plot of a representative IV curve showing the characteristic SCLC domain in HRS while also showing different domains in the LRS. c) Unipolar DC switch cycle of Au only electrode GaS_xO_y/GaS ReRAM where light colors represent the cycles and the saturated color curves represent the average. Inset is a schematic of the Au-only vertical stack ReRAM.

GaS_xO_y/GaS ReRAM shows a slight variation in states over 350 cycles using PVS measurements with an average HRS/LRS ratio of ≈3. In addition, the cumulative distribution function (CDF) plot, shown in Figure 5f, confirms the observation from the endurance measurement where a clear window exists between HRS and LRS with no overlap at any point. In order to assess the potential of our GaS_xO_y/GaS ReRAM for low-power applications, we calculated the energy consumed per SET/RESET operation by numerically integrating the power consumed within the pulse width used. The device consumes, on average, 0.22 and 0.51 nJ to SET and RESET respectively. It is worth noting that the energy consumed by the RESET step excluding the plateau region is on average 0.31 nJ. While this exceeds the desired energy target for these applications, we believe that further optimization of the oxide/semiconductor structure can yield lower energy consumption.

Understanding the performance of ReRAM devices requires not only an examination of their electrical characteristics but also a deeper insight into their switching mechanisms. Different device architectures exhibit varied levels of complexity, which critically influence device performance. The fact that GaS_xO_y/GaS ReRAM has an additional interface which is the oxide/semiconductor one suggests that the switching mechanism is far more complex. In the case of Ti-based Ga_2O_3 resistive switching devices, the commonly suggested mechanism for switching is via the conventional oxygen vacancy filament.[9,12,51] However, in GaS_xO_y/GaS ReRAM, such a simple explanation might not be applicable. First, the oxide layer in GaS_xO_y contains not only oxygen ions and their vacancies but also sulfur ions and their vacancies. While the oxygen ions have a smaller size compared to sulfur ions, which allows them to have higher mobility, determining the dominant conduction-driving ion depends on other factors, such as ions' concentration and the energy barrier for their movement within the oxide. However, a case can be made here for the oxygen ions based on the EELS results in Figure 3g,h. As the sulfur ions are more concentrated near the semiconductor while the oxygen ions are more abundant near the Ti top electrode, it is more likely to have the more mobile oxygen ions that are close to the Ti layer contributing to the filament formation than the far and less mobile sulfur ions.[39] Nevertheless, it is also important to remember that the bottom semiconductor layer might have an active role in the switching. The role of the semiconductor layer is far more complex. While an oxide layer is needed to have switched, it is observed in other literature that the presence of the semiconductor layer improves the stability and endurance of the resistive switching behavior in the device.[39,46]

The complexity of the GaS_xO_y/GaS ReRAM extends to the explanation of the conduction mechanism. Previous reports on Ti-based Ga_2O_3 memristors suggest a space charge limited conduction (SCLC) mechanism in the HRS and ohmic conduction in the LRS.[12,16,51,52] This assertion seems to hold true for the GaS_xO_y/GaS ReRAM (tested on another device with 10 nm GaS_xO_y/GaS), as shown in **Figure 6**a. The HRS shows characteristics of SCLC with an average slope for the ohmic region of ≈1.1, indicating linear *I–V* behavior typical of ohmic conduction. In this region, the current is primarily due to thermally generated carriers within the oxide. As the voltage increases, the device transitions to the trap-filled limit, where injected carriers begin to fill the available trap states in the GaS_xO_y layer. This transition is marked by a change in the slope to ≈1.95, consistent with the Child regime of SCLC, reflecting a quadratic *I–V* relationship ($I \propto V^2$). In this regime, the current is limited by the space charge effects of the injected carriers, confirming the reliability of the SCLC mechanism over 97 DC-IV cycles.

However, the LRS state shows two distinct domains: an ohmic region with a slope of ≈1.01 and an additional region with a slope of ≈1.57. This indicates the presence of at least two conduction mechanisms in the LRS, potentially as a result of the semiconductor layer, as shown in Figure 6b. The initial ohmic region suggests typical ohmic conduction. The intermediate region with a slope of ≈1.57 suggests that the conduction mechanism is influenced by the unique properties of the semiconductor layer. This region may involve more complex interactions within the GaS_xO_y layer, leading to a deviation from purely ohmic behavior and more of a mixed conduction mechanism. The defect density, trap energy levels, and interactions within the GaS_xO_y layer, as well as its interface with the GaS layer, are crucial in defining these mechanisms. The presence of interface states can further influence carrier injection and trapping, contributing to the mixed conduction behavior in the LRS. These findings

© 2024 The Author(s). Advanced Materials Interfaces published by Wiley-VCH GmbH

ADVANCED MATERIALS INTERFACES
Open Access
www.advmatinterfaces.de

21967350, 0, Downloaded from https://onlinelibrary.wiley.com/doi/10.1002/admi.202400481 by University College London UCL Library Services, Wiley Online Library on [28/08/2024]. See the Terms and Conditions (https://onlinelibrary.wiley.com/terms-and-conditions) on Wiley Online Library for rules of use; OA articles are governed by the applicable Creative Commons License

underscore the unique properties and complex conduction mechanisms in GaS_xO_y/GaS ReRAM devices, consistent with previously reported Ga_2O_3-based memristors.

Ti-based top electrode plays a significant role in helping facilitate the formation of a stable conductive filament, which allows the GaS_xO_y/GaS ReRAM to exhibit a resistive switching behavior.[53] To investigate the role of the Ti layer, another set of devices was made without a Ti layer, i.e., consisting of a stack of Au/GaS_xO_y/GaS/Au as shown in Figure 6c. Devices based on this architecture failed to exhibit any stable bipolar switching behavior. Initially, these devices may display one or two promising cycles with current compliance (I_{CC}) set at nano ampere levels but rapidly degrade to a state where no further switching behavior can be observed. Hence, it can be concluded that the presence of Ti is crucial to facilitating the anionic filamentary formation.[39] Nevertheless, an unstable unipolar switching characteristic can be achieved under certain conditions, as shown in Figure 6c. It is unclear what drives such a switching mechanism in this type of device architecture. However, based on previous reports, an Au metallic filament could be responsible for the switching in memristors with only Au contacts.[54,55]

3. Conclusion

In this study, we have successfully demonstrated the capacity to oxidize GaS, a group III monochalcogenide, via a controlled oxygen plasma treatment. Upon close inspection, it was discovered that the oxidation process starts at the surface and progressively moves inward. The resultant oxide is amorphous with a low density and contains some sulfur species doping. Intriguingly, this imperfect oxide composition has proven to be advantageous for ReRAM applications. Our evaluations of ReRAM devices that incorporated this oxide have shown significant potential in combining forming-free operation with hours-long retention, endurance of hundreds of cycles, and sub-nano-Joule energy consumption. With further optimization of the oxidation and careful design of the oxide-semiconductor heterostructure, we expect that such devices can play a significant role in low-power electronics. Moreover, the oxidation method can be explored for applications beyond ReRAMs such as UV photodetectors and gas sensing.

4. Experimental Section

GaS Samples Preparation: GaS flakes were prepared by micromechanical exfoliation from bulk GaS crystal (HQgraphene). SiO_2/Si substrates were first cleaned using acetone, followed by isopropyl alcohol (IPA) and oxygen plasma treatment using an Advanced Vacuum–Vision 320 RIE. The substrates were exposed to 100 W O_2 plasma at 40 sccm and 20 mTorr for 2 min and then transferred into a glovebox with an Ar environment and O_2/H_2O level <0.1 ppm. The flakes were exfoliated immediately on the pretreated substrate. Flakes of interest were identified using an optical microscope. Both exfoliation and optical microscope mapping of flakes were done in the same Ar environment.

GaS Plasma Oxidation: Advanced Vacuum-vision 320 RIE was used to perform the O_2 plasma oxidation. Before placing the substrate, a 100 W O_2 plasma cleaning step was run at 40 sccm and 20 mTorr for 15 min to clean the chamber. To reduce the effect of ambient oxidation, the samples were maintained inside the glovebox until the oxidation chamber was ready. The samples were exposed to ambient air for less than 30 s. For oxidation, 10 W O_2 plasma was used at 10 sccm and 20 mTorr for 10 and 15 min. Post oxidation, the samples were moved back immediately to the glovebox.

Device Fabrication: For device fabrication, a high resistivity (>10000 Ω cm) Si substrate with 285 nm SiO_2 was used to prevent any unwanted current paths during pulse operations due to parasitic capacitances. Substrates were cleaned with acetone and IPA, followed by 100 W O_2 plasma at 40 sccm and 20 mTorr for 2 min. Contacts were patterned by maskless photolithography utilizing a Microtech LW405 laser writer. AZ-5214E image reversal photoresist was chosen for this purpose due to the ease of the lift-off process. Using Kurt J. Lesker PVD 200 Pro, a 50 nm Au bottom electrode was deposited. For lift-off, the substrates were left in an acetone bath overnight. GaS flakes were exfoliated on Si/SiO_2 substrate as described previously. Here, plasma treatment was skipped as it reduces the success rate of flake transfer. Selected flakes, identified by using an optical microscope, were transferred on top of the bottom electrode using a conventional dry transfer technique via Polydimethylsiloxane/polycarbonate (PDMS/PC) stamp.[56] Chloroform was used to remove any residual PC, followed by an IPA cleaning step. While the transfer was done in a glovebox, the chloroform step was done in ambient conditions. Extra care was taken to reduce sample exposure to oxygen during this process. Once transfer and cleaning were completed, the GaS flakes were oxidized as described above. The top electrode was fabricated following the same procedure described for the bottom electrode with the difference that the electrode consisted of 10 nm Ti and 90 nm of Au. Ti was deposited under $\approx 1 \times 10^{-7}$ mTorr pressure to prevent Ti oxidation. For the device shown in Figure 6c, only Au was used.

Electrical Measurements: Keysight/Agilent B1500A semiconductor device parameter analyzer was utilized for all electrical measurements. Voltage was always applied through the common bottom electrode, whereas the top electrode was grounded. A Keysight B1530A Waveform Generator/Fast Measurement Unit (WGFMU) module was used for pulse measurements in conjunction with a Remote-sense and Switch Unit (RSU). All measurements were done in ambient conditions at room temperature.

Raman Spectroscopy Measurements: Raman measurements were performed using a Renishaw inVia micro spectrometer. A 514.5 nm laser was used for all measurements with a 100× magnification lens and a 2400 line mm^{-1} grating. The time and power during the Raman measurement were minimized to avoid unintentional photo-oxidation.

AFM Measurements: The AFM measurements were conducted on a Bruker Dimension Icon AFM. Peak Force Tapping mode coupled with the ScanAsyst algorithm was used for all the measurements.

Ellipsometry Measurements: Ellipsometry measurements were conducted using an EP4 Spectroscopic Imaging Ellipsometer from Park Systems Gmbh. The equipment was equipped with a laser-stabilized Xenon arc lamp and a three-grating monochromator as the spectroscopic light source. This allows for a spectral range between 360 to 1000 nm, with a 5 nm bandwidth of the output line. A polarisation state generator (PSG), consisting of a linear polariser and quarter-wave plate (compensator) was used, to control the state of polarisation of the incident beam. The reflected light is collected through an analyzer and a 50× objective to a 1392 × 1040 pixel CCD camera, which allows for a lateral resolution down to 1 µm. All measurements were performed in the P-A-nulling mode, where the compensator is kept fixed at 45°, and the polariser and analyzer positions were shifted until the signal minimum was reached. Once the nulling condition is satisfied, the sample's ellipsometric angles Δ and ψ at each probing wavelength were recorded.

TEM Measurements: To prepare samples for cross-sectional TEM measurement, GaS flakes were exfoliated on SiO_2/Si substrate as described above. The flakes were then oxidized to the desired time. To provide protection during the lamella preparation process, a double layer consisting of Au and aluminum oxide (AlO_x) was deposited using e-beam evaporation and ALD respectively. During the ALD step, extra care was taken to minimize temperature (which was kept below 150 °C) and time to prevent any modification of the oxide. Lamellas were fabricated using a Dual Beam FIB-SEM system (Carl Zeiss Auriga) equipped with a platinum (Pt) deposition cartridge and nanomanipulator (Kleindiek Nanotechnik). The process started by depositing ≈100 nm of Pt as an additional protection deposited by e-beam evaporation (2 kV). This was subsequently over-

© 2024 The Author(s). Advanced Materials Interfaces published by Wiley-VCH GmbH

laid with a micrometer-thick Pt layer deposited via a gallium ion beam. After the preliminary rough milling stage at 30 kV, the resulting plate, ≈2 µm in thickness, was extracted and attached to the edge of a copper finger in a FIB lift-out grid. The lamella was subsequently thinned using a 15 kV ion beam to minimize ion beam-induced damage, resulting in a final lamella with a thickness under 100 nm. After thinning, the lamella was transferred to the TEM column for observation as soon as possible to minimize potential further oxidation.

The in-plane samples for (S)TEM were prepared by exfoliating GaS flakes as described above. The chosen flakes were then dry transferred using the PDMS/PC transfer method to a silicon nitride (SiN_x) TEM grid with 1 µm diameter holes. Chloroform was used to remove PC residual. The transferred flake was then plasma oxidized as described above.

Transmission electron microscopy (TEM) and scanning TEM (STEM) were conducted on an uncorrected FEI Titan equipped with a Schottky field emission S-FEG source operating at 300 kV. Electron energy-loss spectroscopy (EELS) mapping was executed employing a Quantum Gatan Imaging Filter (GIF) detector, possessing an energy dispersion of 0.5 eV per channel.

To measure the oxide thickness from the TEM images, two flakes per oxidation time were used. To ensure that the TEM images are representative of the flake, at least 5 TEM cross-sectional images were taken per flake at different points. All 20 images were taken using the same magnification to ensure consistency. The images were then processed using purposely made MATLAB code to calculate the oxide thickness in each image. It should be noted that the code requires the user to define the boundaries of each region. To differentiate between the oxide and semiconductor layers, the user manually selects at least ten points at the interface of the layers, and the code employs interpolation to create a detailed 100-point trace along the edge. The thickness measurement is subsequently based on the analysis of these 100 points, ensuring precise delineation between the amorphous oxide layer and the semiconductor.

Acknowledgements

A.A. acknowledges the financial support of the Saudi Arabian Ministry of Education. A.Xh. and A.L. acknowledge funding from EPSRC grant EP/T517793/1. V.N. and X.G. wish to thank the support of the Science Foundation Ireland-funded AMBER Research Centre (Grant No. 12/RC/2278_P2), and the Frontiers for the Future award (Grant No. 20/FFP-A/8950). Furthermore, V.N. and X.G. wish to thank the Advanced Microscopy Laboratory in CRANN for the provision of their facilities. S.H. and I.C. acknowledge funding from EPSRC (EP/T001038/1, EP/V047515/1, EP/N509620/1, EP/R513180/1).

Conflict of Interest

The authors declare no conflict of interest.

Data Availability Statement

The data that support the findings of this study are available from the corresponding author upon reasonable request.

Keywords

2D material, oxidation, gallium sulfide, gallium oxide, neuromorphic, ReRAM

Received: May 31, 2024
Revised: July 30, 2024
Published online:

[1] Y. Liao, Z. Zhang, Z. Gao, Q. Qian, M. Hua, *ACS Appl. Mater. Interfaces.* **2020**, *12*, 30659.
[2] J. Su, R. Guo, Z. Lin, S. Zhang, J. Zhang, J. Chang, Y. Hao, *J. Phys. Chem. C.* **2018**, *122*, 24592.
[3] H. He, R. Orlando, M. A. Blanco, R. Pandey, E. Amzallag, I. Baraille, M. Rérat, *Phys. Rev. B.* **2006**, *74*, 195123.
[4] M. Orita, H. Ohta, M. Hirano, H. Hosono, *Appl. Phys. Lett.* **2000**, *77*, 4166.
[5] H. H. Tippins, *Phys. Rev.* **1965**, *140*, A316.
[6] M. Higashiwaki, K. Sasaki, A. Kuramata, T. Masui, S. Yamakoshi, *Appl. Phys. Lett.* **2012**, *100*, 123511.
[7] M. Bartic, M. Ogita, M. Isai, C.-L. Baban, H. Suzuki, *J. Appl. Phys.* **2007**, *102*, 023709.
[8] M. Ogita, K. Higo, Y. Nakanishi, Y. Hatanaka, *Appl. Surf. Sci.* **2001**, *175–176*, 721.
[9] D. Y. Guo, Y. P. Qian, Y. L. Su, H. Z. Shi, P. G. Li, J. T. Wu, S. L. Wang, C. Cui, W. H. Tang, *AIP Adv.* **2017**, *7*, 065312.
[10] N. Masaoka, Y. Hayashi, T. Tohei, A. Sakai, *Jpn. J. Appl. Phys.* **2023**, *62*, SC1035.
[11] D. Cui, Y. Du, Z. Lin, M. Kang, Y. Wang, J. Su, J. Zhang, Y. Hao, J. Chang, *IEEE Electron Device Lett.* **2023**, *44*, 237.
[12] R. T. Velpula, B. Jain, H. P. T. Nguyen, *Nanotechnology.* **2022**, *34*, 075201.
[13] Z. Yang, J. Wu, P. Li, Y. Chen, Y. Yan, B. Zhu, C. S. Hwang, W. Mi, J. Zhao, K. Zhang, R. Guo, *Ceram. Int.* **2020**, *46*, 21141.
[14] D. Y. Guo, Z. P. Wu, Y. H. An, P. G. Li, P. C. Wang, X. L. Chu, X. C. Guo, Y. S. Zhi, M. Lei, L. H. Li, W. H. Tang, *Appl. Phys. Lett.* **2015**, *106*, 042105.
[15] S. Wang, C. He, J. Tang, R. Yang, D. Shi, G. Zhang, *Chin. Phys. B.* **2019**, *28*, 097201.
[16] Y. Xu, J. Zhang, X. Han, X. Wang, C. Ye, W. Mu, Z. Jia, K. Qian, *ACS Appl. Mater. Interfaces.* **2023**, *15*, 25831.
[17] E. Swinnich, M. N. Hasan, K. Zeng, Y. Dove, U. Singisetti, B. Mazumder, J. H. Seo, *Adv. Electron. Mater.* **2019**, *5*, 1800714.
[18] Y. Lu, J. Chen, T. Chen, Y. Shu, R. J. Chang, Y. Sheng, V. Shautsova, N. Mkhize, P. Holdway, H. Bhaskaran, J. H. Warner, *Adv. Mater.* **2020**, *32*, 1906958.
[19] T. Jin, Y. Zheng, J. Gao, Y. Wang, E. Li, H. Chen, X. Pan, M. Lin, W. Chen, *ACS Appl. Mater. Interfaces.* **2021**, *13*, 10639.
[20] S. Lai, S. Byeon, S. K. Jang, J. Lee, B. H. Lee, J. H. Park, Y. H. Kim, S. Lee, *Nanoscale.* **2018**, *10*, 18758.
[21] M. J. Mleczko, C. Zhang, H. R. Lee, H. H. Kuo, B. Magyari-Kope, R. G. Moore, Z. X. Shen, I. R. Fisher, Y. Nishi, E. Pop, *Sci. Adv.* **2017**, *3*, e1700481.
[22] B. Chamlagain, Q. Cui, S. Paudel, M. M.-C. Cheng, P.-Y. Chen, Z. Zhou, *2D Mater.* **2017**, *4*, 031002.
[23] T. Li, T. Tu, Y. Sun, H. Fu, J. Yu, L. Xing, Z. Wang, H. Wang, R. Jia, J. Wu, C. Tan, Y. Liang, Y. Zhang, C. Zhang, Y. Dai, C. Qiu, M. Li, R. Huang, L. Jiao, K. Lai, B. Yan, P. Gao, H. Peng, *Nat. Electron.* **2020**, *3*, 473.
[24] N. Peimyoo, M. D. Barnes, J. D. Mehew, A. De Sanctis, I. Amit, J. Escolar, K. Anastasiou, A. P. Rooney, S. J. Haigh, S. Russo, M. F. Craciun, F. Withers, *Sci. Adv.* **2019**, *5*, eaau0906.
[25] S. Yang, Y. Li, X. Wang, N. Huo, J. B. Xia, S. S. Li, J. Li, *Nanoscale.* **2014**, *6*, 2582.
[26] D. J. Late, B. Liu, J. Luo, A. Yan, H. S. Matte, M. Grayson, C. N. Rao, V. P. Dravid, *Adv. Mater.* **2012**, *24*, 3549.
[27] D. A. Bandurin, A. V. Tyurnina, G. L. Yu, A. Mishchenko, V. Zolyomi, S. V. Morozov, R. K. Kumar, R. V. Gorbachev, Z. R. Kudrynskyi, S. Pezzini, Z. D. Kovalyuk, U. Zeitler, K. S. Novoselov, A. Patane, L. Eaves, I. V. Grigorieva, V. I. Fal'ko, A. K. Geim, Y. Cao, *Nat. Nanotechnol.* **2017**, *12*, 223.
[28] S. R. Tamalampudi, Y. Y. Lu, U. R. Kumar, R. Sankar, C. D. Liao, B. K. Moorthy, C. H. Cheng, F. C. Chou, Y. T. Chen, *Nano Lett.* **2014**, *14*, 2800.

© 2024 The Author(s). Advanced Materials Interfaces published by Wiley-VCH GmbH

21967350, 0, Downloaded from https://onlinelibrary.wiley.com/doi/10.1002/admi.202400481 by University College London UCL Library Services, Wiley Online Library on [28/08/2024]. See the Terms and Conditions (https://onlinelibrary.wiley.com/terms-and-conditions) on Wiley Online Library for rules of use; OA articles are governed by the applicable Creative Commons License

[29] T. E. Beechem, B. M. Kowalski, M. T. Brumbach, A. E. McDonald, C. D. Spataru, S. W. Howell, T. Ohta, J. A. Pask, N. G. Kalugin, *Appl. Phys. Lett.* **2015**, *107*, 173103.
[30] C. Schmidt, M. Rahaman, D. R. T. Zahn, *Nanotechnology.* **2021**, *33*, 045702.
[31] C. H. Ho, S. L. Lin, *J. Appl. Phys.* **2006**, *100*, 083508.
[32] I. Chircă, A. AlMutairi, B. Achinuq, R. Cai, S. J. Haigh, S. Hofmann, *2D Mater.* **2024**, *11*, 045001.
[33] G. E. Jellison, F. A. Modine, *Appl. Phys. Lett.* **1996**, *69*, 371.
[34] Y. Gutierrez, M. M. Giangregorio, S. Dicorato, F. Palumbo, M. Losurdo, *Front. Chem.* **2021**, *9*, 781467.
[35] W. Liu, J. He, X. Zhu, T. Huang, X. Chen, Y. Zheng, L. Chen, R. Zhang, *Thin Solid Films* **2023**, *766*, 139655.
[36] H. Yang, Y. Liu, X. Luo, Y. Li, D.-S. Wuu, K. He, Z. C. Feng, *Superlattices Microstruct.* **2019**, *131*, 21.
[37] C. V. Ramana, E. J. Rubio, C. D. Barraza, A. M. Gallardo, S. McPeak, S. Kotru, J. T. Grant, *J. Appl. Phys.* **2014**, *115*, 043508.
[38] S. Ilhom, A. Mohammad, D. Shukla, J. Grasso, B. G. Willis, A. K. Okyay, N. Biyikli, *ACS Appl. Mater. Interfaces.* **2021**, *13*, 8538.
[39] L. Liu, Y. Li, X. Huang, J. Chen, Z. Yang, K. H. Xue, M. Xu, H. Chen, P. Zhou, X. Miao, *Adv. Sci.* **2021**, *8*, e2005038.
[40] Y. Chen, *IEEE Trans. Electron Devices.* **2020**, *67*, 1420.
[41] D. Ielmini, H. S. P. Wong, *Nat. Electron.* **2018**, *1*, 333.
[42] J. J. Yang, D. B. Strukov, D. R. Stewart, *Nat. Nanotechnol.* **2013**, *8*, 13.
[43] R. Waser, M. Aono, *Nat. Mater.* **2007**, *6*, 833.
[44] E. Ambrosi, A. Bricalli, M. Laudato, D. Ielmini, *Faraday Discuss.* **2019**, *213*, 87.
[45] L. Yin, R. Cheng, Z. Wang, F. Wang, M. G. Sendeku, Y. Wen, X. Zhan, J. He, *Nano Lett.* **2020**, *20*, 4144.
[46] Y. Li, S. Chen, Z. Yu, S. Li, Y. Xiong, M. E. Pam, Y. W. Zhang, K. W. Ang, *Adv. Mater.* **2022**, *34*, 2201488.
[47] A. Xhameni, A. AlMutairi, A. Lombardo, in 2023 IEEE Nanotechnology Materials and Devices Conference (NMDC), **2023**.
[48] X. Sheng, C. E. Graves, S. Kumar, X. Li, B. Buchanan, L. Zheng, S. Lam, C. Li, J. P. Strachan, *Adv. Electron. Mater.* **2019**, *5*, 1800876.
[49] T. Diokh, E. Le-Roux, S. Jeannot, C. Cagli, V. Jousseaume, J.-F. Nodin, M. Gros-Jean, C. Gaumer, M. Mellier, J. Cluzel, C. Carabasse, P. Candelier, B. De Salvo, *Thin Solid Films.* **2013**, *533*, 24.
[50] C. Yang Yin, B. Govoreanu, L. Goux, R. Degraeve, A. Fantini, G. S. Kar, D. J. Wouters, G. Groeseneken, J. A. Kittl, M. Jurczak, L. Altimime, *IEEE Trans. Electron Devices.* **2012**, *59*, 3243.
[51] L. Zhang, H. Yu, L. Xiong, W. Zhu, L. Wang, *J. Mater. Sci.: Mater. Electron.* **2019**, *30*, 8629.
[52] K. Sato, Y. Hayashi, N. Masaoka, T. Tohei, A. Sakai, *Sci. Rep.* **2023**, *13*, 1261.
[53] H. R. J. Cox, M. Buckwell, W. H. Ng, D. J. Mannion, A. Mehonic, P. R. Shearing, S. Fearn, A. J. Kenyon, *APL Mater.* **2021**, *9*, 111109.
[54] Y. Shen, W. Zheng, K. Zhu, Y. Xiao, C. Wen, Y. Liu, X. Jing, M. Lanza, *Adv. Mater.* **2021**, *33*, 2103656.
[55] S. Chen, M. R. Mahmoodi, Y. Shi, C. Mahata, B. Yuan, X. Liang, C. Wen, F. Hui, D. Akinwande, D. B. Strukov, M. Lanza, *Nat. Electron.* **2020**, *3*, 638.
[56] D. G. Purdie, N. M. Pugno, T. Taniguchi, K. Watanabe, A. C. Ferrari, A. Lombardo, *Nat. Commun.* **2018**, *9*, 5387.

© 2024 The Author(s). Advanced Materials Interfaces published by Wiley-VCH GmbH

21967350, 0, Downloaded from https://onlinelibrary.wiley.com/doi/10.1002/admi.202400481 by University College London UCL Library Services, Wiley Online Library on [28/08/2024]. See the Terms and Conditions (https://onlinelibrary.wiley.com/terms-and-conditions) on Wiley Online Library for rules of use; OA articles are governed by the applicable Creative Commons License